

Supporting Information

Ternary PtIrNi Catalysts for Efficient Electrochemical Ammonia Oxidation

Yi Li,^{†,‡} Xing Li,^{§,||} Hemanth Somarajan Pillai,[⊥] Judith Lattimer,[∇] Nadia Mohd Adli,[†] Stavros Karakalos,[#] Mengjie Chen,[†] Lin Guo,[†] Hui Xu,[∇] Juan Yang,^{*,‡} Dong Su,^{*,§} Hongliang Xin,^{*,⊥} and Gang Wu^{*,†}

[†]Department of Chemical and Biological Engineering, University at Buffalo, The State University of New York, Buffalo, NY 14260, USA.

[‡]School of Materials Science and Engineering, Jiangsu University, Zhenjiang, 212013, China.

[⊥]Department of Chemical Engineering, Virginia Polytechnic Institute and State University, Blacksburg, Virginia 24061, USA.

[∇]Giner Inc., Newton, MA 02466, United States

[§]Center for Functional Nanomaterials, Brookhaven National Laboratory, Upton, New York 11973, USA.

^{||}Key Laboratory of Materials Physics, School of Physics, Zhengzhou University, Zhengzhou, 450052, China.

[#]Department of Chemical Engineering, University of South Carolina, Columbia, South Carolina 29208, USA

*Corresponding authors

*gangwu@buffalo.edu (G. Wu); *yangjuan6347@ujs.edu.cn (J. Yang); *dongsu88@yahoo.com (D. Su); *hxin@vt.edu (H. Xin).

Experimental Details

Computational Details

Figure S1 to S27

Table S1 to S5

References

Experimental Details

Catalyst Synthesis

(1) Preparation of porous SiO₂ and CNT-COOH: Porous SiO₂ was prepared by sol-gel process adapted from the literature.^{1, 2} In a typical procedure, the poly(ethylene oxide) (Mw=10⁵, Sigma Aldrich, 12.5 g) was dissolved in 1.0 M HNO₃ (125 g) in a round-bottom flask (500-mL size) at room temperature. Then, tetraethyl orthosilicate (98%, Sigma Aldrich, 81.25 g) was added to the solution, sealed and stirred on a stir plate at room temperature for 30 min. Subsequently, the flask was transferred to an oven preheated to 40°C and stood for 2.5 days. The resulted monolithic white gel was broken into small pieces (< 5 mm) and immersed in 300 ml of deionized (DI) H₂O to soak out the acid remained in the gel. The solvent was changed every 2 hours. The 4th solvent was 0.045 M NH₄OH/H₂O. The gel particles were then rinsed with DI H₂O and dried at 40°C for 24 h, and then at 100°C for 12 h. The dried gel particles were heated in air with a temperature ramping rate of 1.5°C/min up to 600°C, kept at 600°C for 12 h. Carbon nanotube (CNT) was functionalized with carboxyl groups marked as (CNT-COOH) using a mixed acid solution of DI H₂O/HNO₃/H₂SO₄ (V/V/V=4:1:3) at 100°C for 4 h under vigorous stirring and reflux condition.³

(2) Preparation of PtIrNi nanoparticle alloys deposited on binary support of porous SiO₂ and CNT-COOH: To prepare the compounds, the precious-group-metal (PGM, Pt or Pt-Ir) loadings of 10 wt% for all the prepared catalysts were deposited on the binary support of porous SiO₂ and CNT-COOH. The synthesis of different materials (e.g., PtIr/SiO₂-CNT-COOH, PtNi/SiO₂-CNT-COOH, and PtIrNi₁/SiO₂-CNT-COOH) has been accomplished by a sonochemical-assisted reduction method using strong reducing agent of sodium borohydride. Typically, the grinded porous SiO₂ was dispersed in 30 mL of 0.01 M NaOH and ultrasonicated for 30 min. Subsequently, the SiO₂ was centrifuged and re-dispersed in 30 mL of DI H₂O and this washing step was repeated

twice, and then re-dispersed in 20 mL of DI H₂O for the adsorption of metal ions. Then, a certain amount of CNT-COOH was added into the obtained SiO₂ dispersion and ultrasonicated for 30 min to make a homogeneous dispersion. The 0.1 M precursors of potassium chloroplatinate, chloro-iridic acid, and nickel nitrate aqueous solution were added into the dispersion one by one under ultrasonication conditions. To make a good adsorption of metal ions onto the supports, the dispersion including metal ions was continuously ultrasonicated for 1.0 h and then magnetically stirred for additional 1.0 h. Before sodium borohydride reduction, the dispersion was placed in an ultrasonic environment, and then 0.5 M sodium borohydride aqueous solution was dropped wisely into the dispersion, and obvious bubbles can be seen during the reaction, indicating the violent reduction reaction between the reducing agent and the metal ions. After all sodium borohydride aqueous solution was added into the dispersion, ultrasonic reaction for additional 1.0 h was needed to make sure a complete reduction of the metal ions. After the reaction was finished, the products were washed with DI H₂O for several times until no Cl⁻ could be detected by AgNO₃ solution and dried at 60°C in a vacuum oven for overnight. The as-prepared catalysts are designed as PtIrNi_x/SiO₂-CNT-COOH (x=1, 2 or 3). Molar ratios of Pt:Ir:Ni in the PtIrNi_x/SiO₂-CNT-COOH (x=1, 2 or 3) catalysts are confined to 9:1:1, 9:1:3, and 9:1:9, correspondingly. Other samples (e.g., Pt/CeO₂-CNT-COOH, PtIr/SiO₂-CNT-COOH and PtNi/SiO₂-CNT-COOH in molar ratio of Pt:Ir and Pt:Ni = 9:1, and Pt₅Ir₅/SiO₂-CNT-COOH in molar of Pt:Ir = 1:1) were prepared using a similar procedure and the corresponding metal precursors.

Physical Characterization

The morphology and structure characterization were performed on JEOL JEM-2100F at an accelerating voltage of 200 kV to obtain bright field and high-resolution transmission electron microscopy (HRTEM) images. The high angle annular dark field (HAADF) scanning transmission

electron microscopy (STEM) images and elemental mappings were conducted on a high-resolution analytical scanning/transmission electron microscope (S/TEM, FEI Talos F200X, operating at 200 keV) equipped with a four-quadrant 0.9-sr energy-dispersive X-ray spectrometer (EDS). The crystalline phases of the catalysts were investigated by employing powder X-ray diffraction (XRD) on a Rigaku Ultima IV diffractometer with Cu K α X-rays. The N₂ isothermal adsorption/desorption was conducted on a Micromeritics TriStar II. Before tests, samples were degassed at 150°C for 5 h under vacuum. X-ray photoelectron spectroscopy (XPS) was carried out using a Kratos AXIS Ultra DLD XPS system equipped with a hemispherical energy analyzer and a monochromatic Al K α source.

Electrochemical Measurements

An electrochemical workstation (CHI760b) coupled with a rotating disk electrode (RDE, PINE, AFMSRCE 3005) in a three-electrode cell was employed to perform electrochemical measurements. A graphite rod and an Hg/HgO (filled with 1.0 M KOH) electrode were utilized as the counter and reference electrodes, respectively. An Ag/AgCl (KCl-sat.) electrode bought from Metrohm was used as the reference electrode under high testing temperatures (0-80°C). The reference electrode was calibrated to a reversible hydrogen electrode (RHE) in the same electrolyte before each test. A rotating ring-disk electrode (RRDE) with a disk diameter of 5.6 mm and an RDE electrode with a disk diameter of 5.0 mm covered by a thin film of the catalyst were employed as the working electrode at room and high temperatures (0-80°C), respectively. To compare the AOR activity with our prepared catalysts, the commercial Pt/C (Sigma-Aldrich, 20 wt%) and PtIr/C catalysts (Premetek, 40 wt%, Pt:Ir molar ratio 1:1) were also conducted at similar testing condition. To prepare the working electrode, 2 mg catalyst was ultrasonically dispersed in a 1.0 mL mixture of isopropanol and Nafion (6 μ L, 5 wt.%) solution to form an ink. Subsequently, the

ink was drop-casted on the disk electrode with a designed loading of $20 \mu\text{g}_{\text{PGM}} \text{cm}^{-2}$ and dried at room temperature to yield a thin-film electrode. The catalyst-coated disk working electrode was subjected to cyclic voltammetry (CV) in Ar-saturated 1.0 M KOH at a scan rate of 50 mV s^{-1} to activate the catalysts, and the recorded CV curves is at a scan rate of 20 mV s^{-1} . The electrocatalytic activity of the catalyst for AOR was characterized by CV measurements in 1.0 M KOH + 0.1 M NH_3 solution at a scan rate of 5 mV s^{-1} with an RDE rotating speed of 900 rpm. AOR stability tests were recorded in 1.0 M KOH + 0.1 M NH_3 electrolyte before and after 2000 potential cycles. The CV cycles were measured in the potential range of 0.05–0.7 V in Ar-saturated 1.0 M KOH at a scanning rate of 500 mV s^{-1} . The NH_3 loaded electrolyte solutions were prepared by mixing NH_3 solution (28.0–30.0%, ACS-Reagenz) with KOH and DI water. In the ammonia oxidation tests, a reduction potential (-0.8 V vs. SHE) holding for 100 s was used to recover the catalyst when the catalyst was used in subsequent tests (often the CVs and i-t curves of the same catalyst). For the experiments of ammonia concentration and temperature effects, a fresh electrode was used for every single test and a similar electrochemical cleaning procedure was followed. Electrochemical impedance spectroscopy (EIS) measurements were conducted at the catalysts' corresponding open circuit potential in the frequency range of 10^{-2} to 10^6 Hz with 10 mV sinusoidal perturbations and 12 steps per decade in 1.0 M KOH solution. In addition, all the remained CV curves were used the same potential cycling protocols to describe the different AOR catalysts.

Computational Details

DFT Calculations

DFT calculations were performed using Vienna Ab Initio Simulation Package (VASP) with projector augmented wave pseudopotentials. A plane wave energy cutoff of 500 eV was used and calculations were performed at the GGA level using RPBE. For systems containing nickel spin

polarized calculations were performed otherwise non-spin polarized calculations were performed. Slabs were separated by a vacuum of 30 Å and a Monkhorst-Pack mesh of $6 \times 6 \times 1$ was used to sample the Brillouin zone. Methfessel-Paxton smearing was used with a smearing parameter of 0.1 eV and energies were extrapolated to $kT = 0$ eV. For bulk systems, a mesh of $8 \times 8 \times 8$ was used with Methfessel-Paxton smearing and a smearing parameter of 0.1 eV. All the energetics and thermodynamics shown in figure 7a of the main text were calculated within the constant potential framework.⁴ Solvation was included through the use of VASPsol.^{5, 6} For solvation the dielectric constant was set to 78.4 while the Debye screening length was set to 3 Å. The surface tension parameter (τ) was set to 0 and precision was set at “Accurate”.

The energetics and thermodynamics for the Pt(100) system have been previously calculated and thus these numbers were used. In order to create the slabs for the Pt₃Ir and Pt₃IrNi systems a bulk Pt₃Ir was first optimized and a lattice constant of 3.963 Å was calculated. This lattice constant was used to generate a 2×2 supercell with 7 layers. Adsorbates were appended such that the slab was symmetric. The middle three slab layers were fixed during geometry optimization, while the positions of the other layers and adsorbates were optimized till the maximum force was less than 0.03 eV/Å.

As mentioned in the main text such a bulk alloy will have two (100) terminations, both terminations were considered. For the Pt₃IrNi system one of the Pt atoms on the Pt₃Ir surface was replaced with a Ni atom. For the calculation of the free energy the zero-point energy and entropy corrections from previous work on the Pt(100) system was used.⁷

Group Orbital Calculations

Group orbitals were calculated through equation S1 where the kets indicate the d orbital states and the coefficients are the coupling coefficients between the p_z orbital and the respective d orbital.

These coefficients were calculated from the Slater-Koster table.⁸ The density of states (DOS) was then projected on these group orbitals to understand the trend that was observed, this is plotted in **Figure 8b** of the main text. Bond distances between the nitrogen atom of the *NH adsorbate and the surface atoms were used to calculate the coefficients. All surfaces that were used to calculate the group orbital had coadsorbed *OH and thus the bridge *NH structure was used. These structures are indicated in **Figure 8b**.

$$|g\rangle = \frac{V_{p_z,xy} |xy\rangle + V_{p_z,x^2-y^2} |x^2 - y^2\rangle + V_{p_z,z^2} |z^2\rangle + V_{p_z,zy} |zy\rangle + V_{p_z,zx} |zx\rangle}{(V_{p_z,xy}^2 + V_{p_z,x^2-y^2}^2 + V_{p_z,z^2}^2 + V_{p_z,zy}^2 + V_{p_z,zx}^2)^{\frac{1}{2}}} \quad (\text{S1})$$

Supplementary Figures

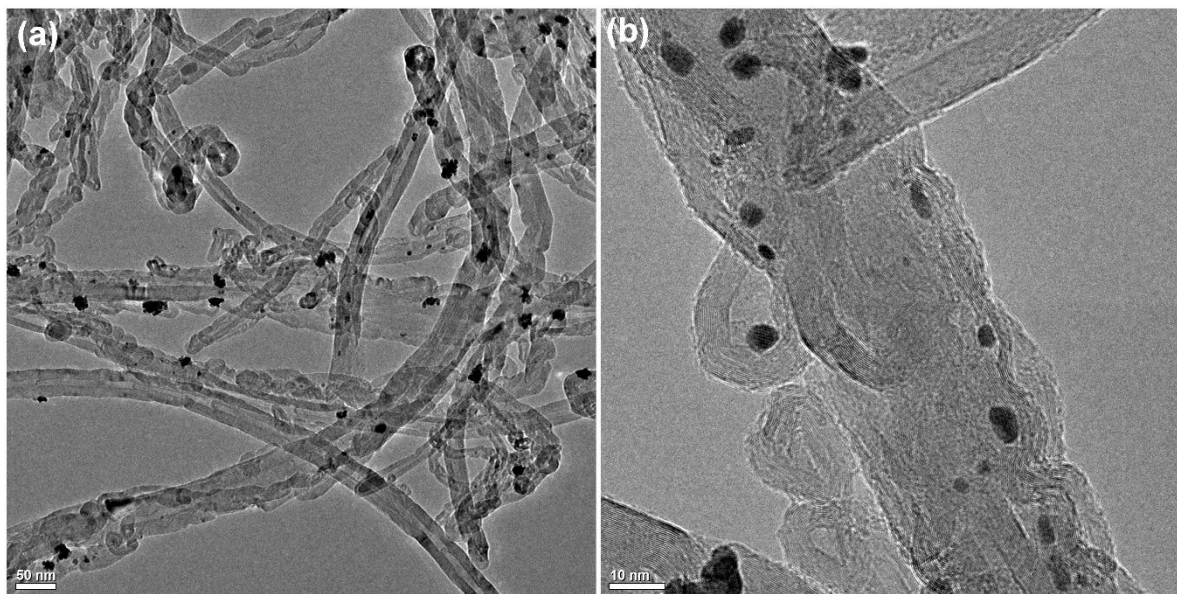


Figure S1. Morphology, structure and composition of the PtIr/SiO₂-CNT-COOH, (a, b) TEM images show SiO₂ integrated with CNTs supporting bimetallic PtIr nanoparticles.

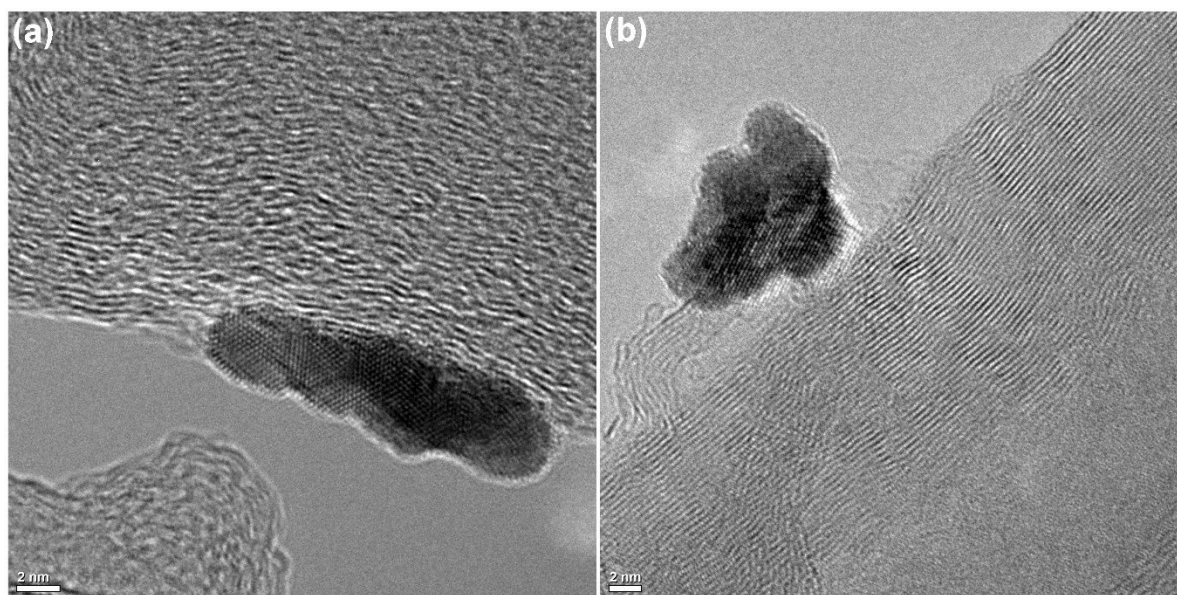


Figure S2. Morphology, structure and composition of the PtIr/SiO₂-CNT-COOH, (a, b) HR-TEM images show that PtIr alloy crystalline lattice spacing of 0.225 nm and CNT layer spacing of 0.320 nm, respectively.

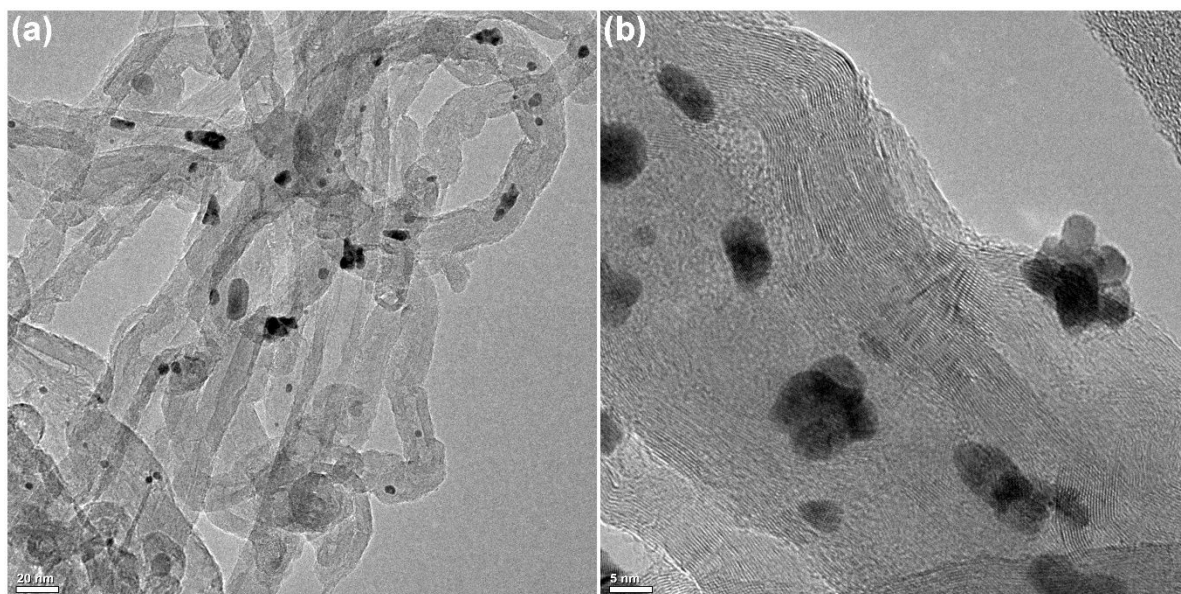


Figure S3. Morphology, structure and composition of the PtIrNi₁/SiO₂-CNT-COOH, (a, b) HR-TEM images show SiO₂ integrated with CNTs supporting ternary PtIrNi nanoparticles.

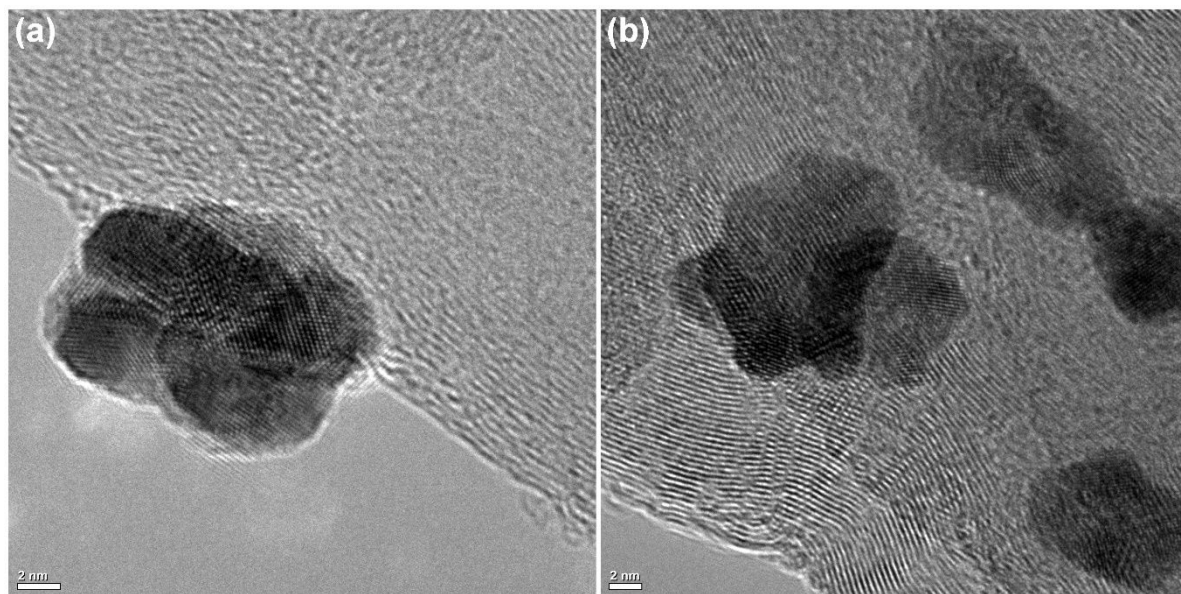


Figure S4. Morphology, structure and composition of the PtIrNi₁/SiO₂-CNT-COOH, (a, b) HR-TEM images show that PtIrNi alloy crystalline lattice spacing of 0.220 nm and CNT layer spacing of 0.320 nm, respectively.

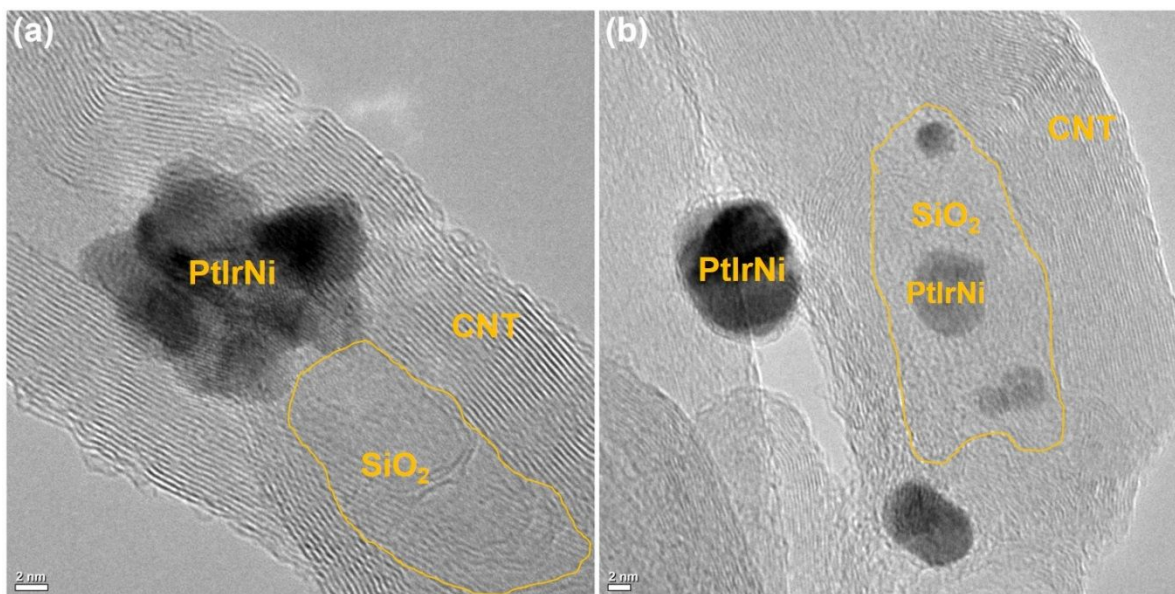


Figure S5. Morphology, structure and composition of the PtIrNi₁/SiO₂-CNT-COOH, (a, b) HR-TEM images show that clear interfaces between SiO₂ and PtIrNi which are the key active sites contribution.

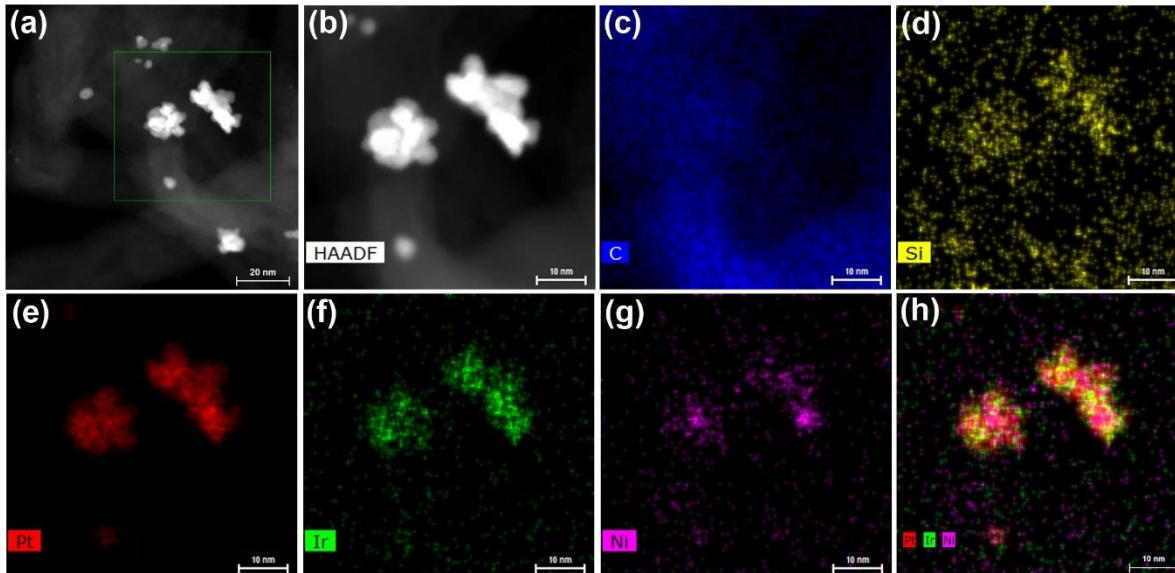


Figure S6. Morphology, structure and composition of the PtIrNi₁/SiO₂-CNT-COOH. (a, b) HAAD-STEM images, and the corresponding elemental mappings of (c) C, (d) Si, (e) Pt, (f) Ir, (g) Ni, and (h) integrated mapping of Pt, Ir, and Ni suggest the formation of PtIrNi alloys.

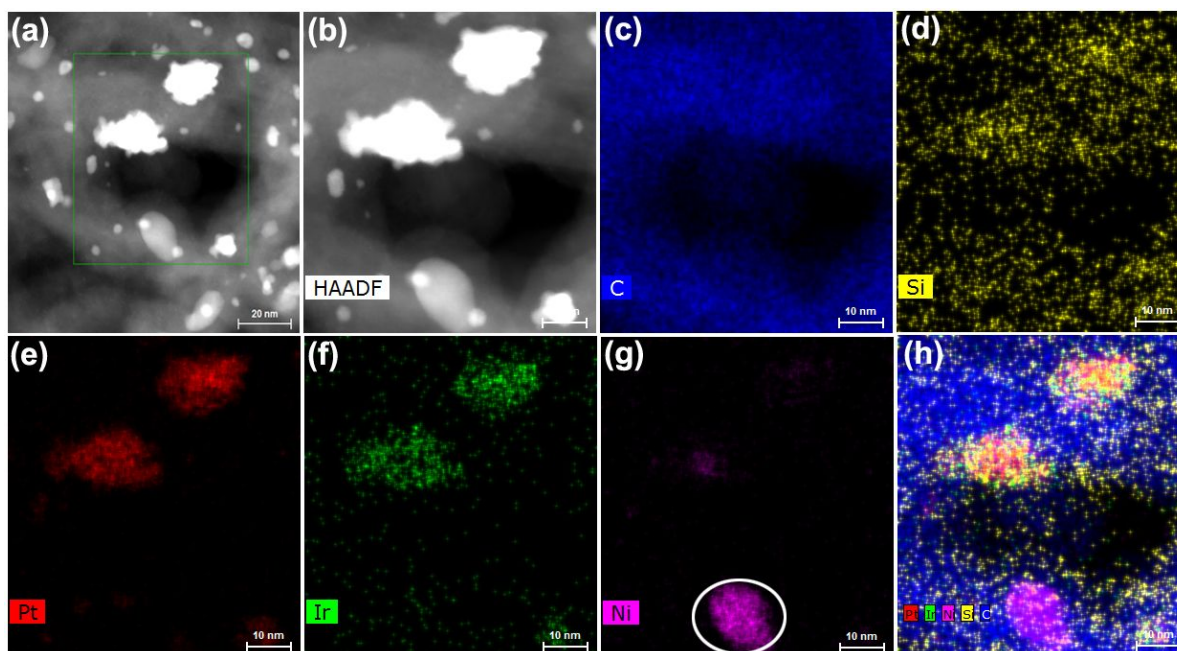


Figure S7. Morphology, structure and composition of the PtIrNi₁/SiO₂-CNT-COOH. (a, b) HAADF-STEM images, and the corresponding elemental mappings of (c) C, (d) Si, (e) Pt, (f) Ir, (g) Ni, and (h) integrated mapping of Pt, Ir, Ni, Si, and C. Few Ni nanoparticles in the sample suggest the incomplete alloy state of the final catalyst.

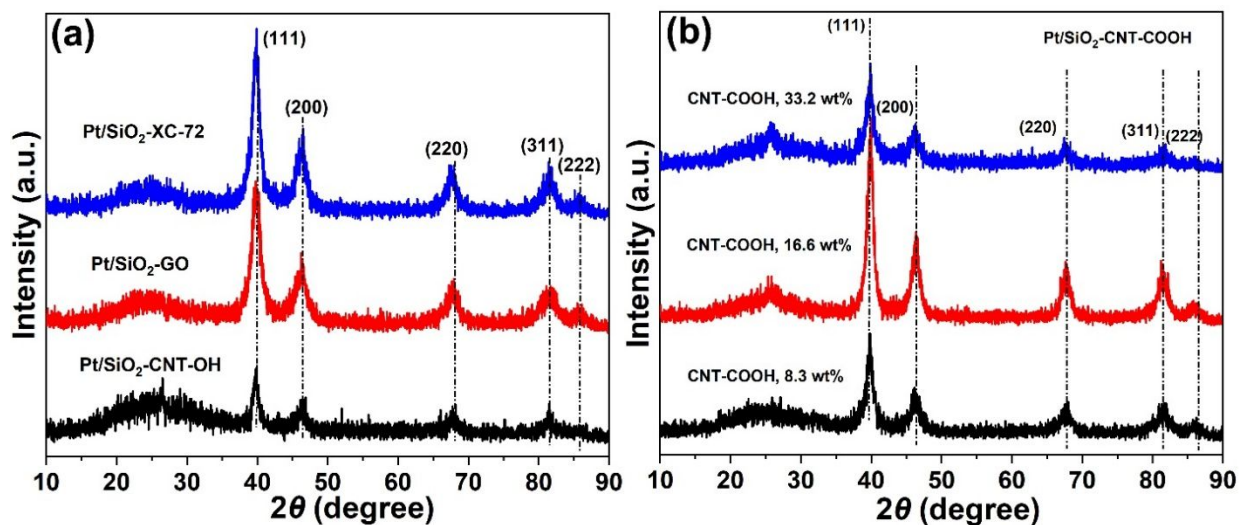


Figure S8. XRD patterns of the (a) Pt/SiO₂-CNT-OH, Pt/SiO₂-GO, and Pt/SiO₂-XC-72, and (b) Pt/SiO₂-CNT-COOH with different carbon contents (8.3 wt%, 16.6 wt%, and 33.2 wt%). The XRD pattern results indicate the successful deposition of Pt nanoparticles on different supports.

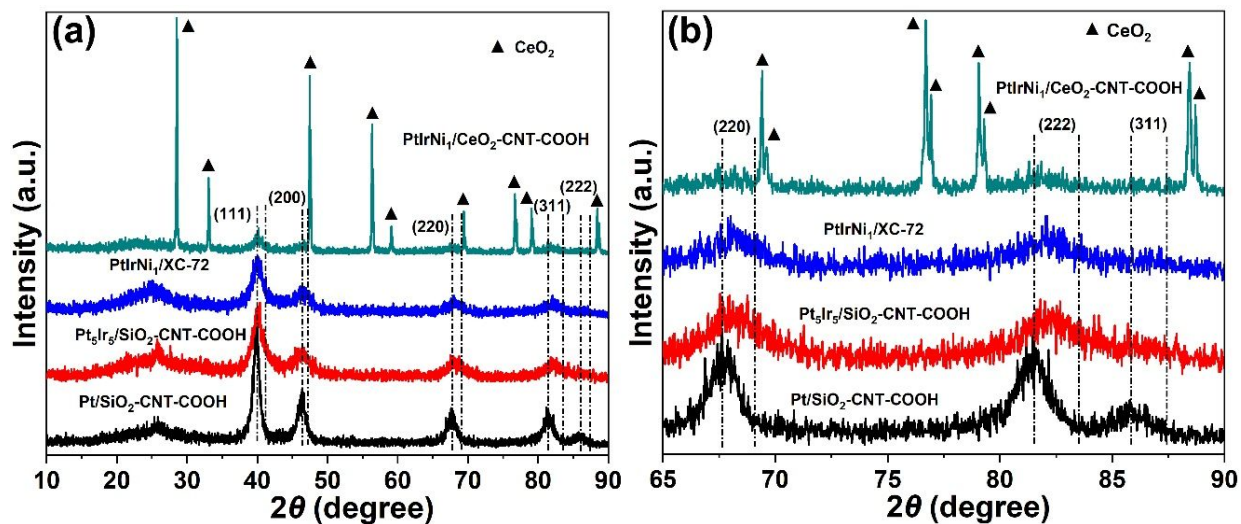


Figure S9. XRD patterns of the (a) Pt/SiO₂-CNT-COOH, Pt₅Ir₅/SiO₂-CNT-COOH, PtIrNi₁/XC-72, and PtIrNi₁/CeO₂-CNT-COOH, and (b) the corresponding XRD patterns with enlarged region of 2θ from 65° to 90°. The XRD pattern results suggest the alloy state of these catalysts using Pt/SiO₂-CNT-COOH as the reference for pure Pt nanoparticles.

Table S1. Elemental quantification (at.%) determined by XPS for different Pt-based catalysts.

Samples	C (at.%)	O (at.%)	Si (at.%)	Pt (at.%)	Ir (at.%)	Ni (at.%)
Commercial Pt/C	89.6	7.3		3.1		
Pt/SiO ₂ -CNT-COOH	57.8	28.7	12.3	1.2		
PtIr/SiO ₂ -CNT-COOH	64.3	23.5	10.7	1.4	0.1	
PtIrNi ₁ /SiO ₂ -CNT-COOH	87.2	7.4	2.3	2.5	0.3	0.3
PtIrNi ₁ /XC-72	96.7	2.0		0.9	0.1	0.3

Table S2. Binding energy comparison of high-resolution Pt 4f for different Pt-based catalysts, Δ_1 and Δ_2 represents binding energy differences between commercial Pt/C with other Pt-based catalysts for Pt 4f_{5/2} and Pt 4f_{7/2}, respectively.

Samples	Pt 4f _{5/2} (eV)	Δ_1 (eV)	Pt 4f _{7/2} (eV)	Δ_2 (eV)
Commercial Pt/C	75.34		72.10	
Pt/SiO ₂ -CNT-COOH	74.75	-0.59	71.39	-0.71
PtIr/SiO ₂ -CNT-COOH	74.77	-0.57	71.47	-0.63
PtIrNi ₁ /SiO ₂ -CNT-COOH	74.83	-0.49	71.47	-0.63
PtIrNi ₁ /XC-72	74.89	-0.45	71.59	-0.51

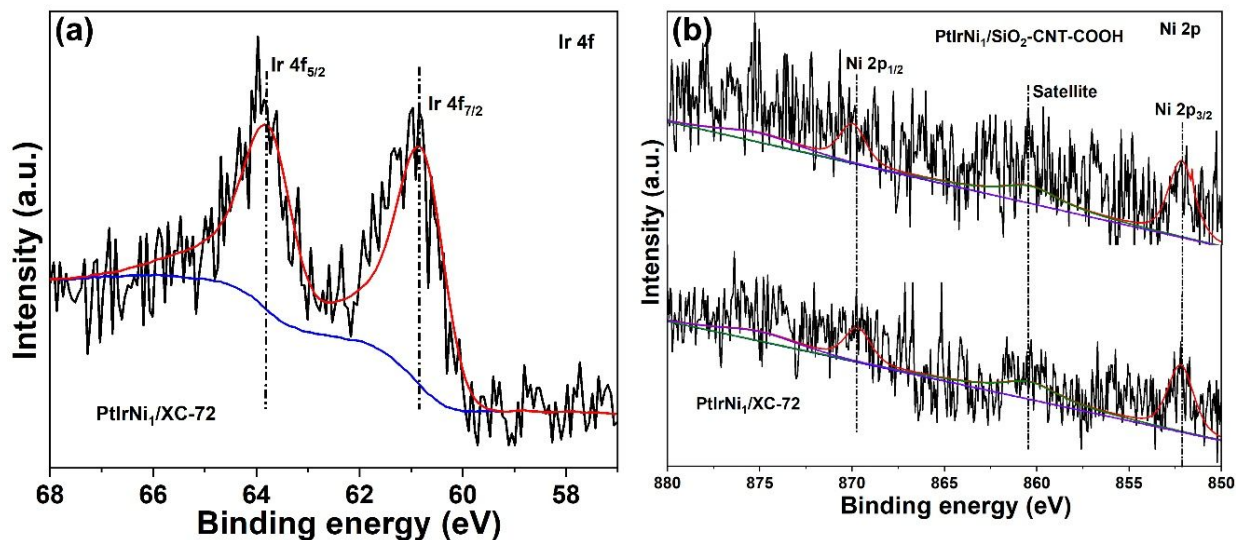


Figure S10. High-resolution XPS data. (a) Ir 4f of the PtIrNi₁/XC-72, and (b) Ni 2p of the PtIrNi₁/SiO₂-CNT-COOH and PtIrNi₁/XC-72. This suggests the possible shifts of banding energies of alloyed Ir and Ni in the corresponding catalysts.

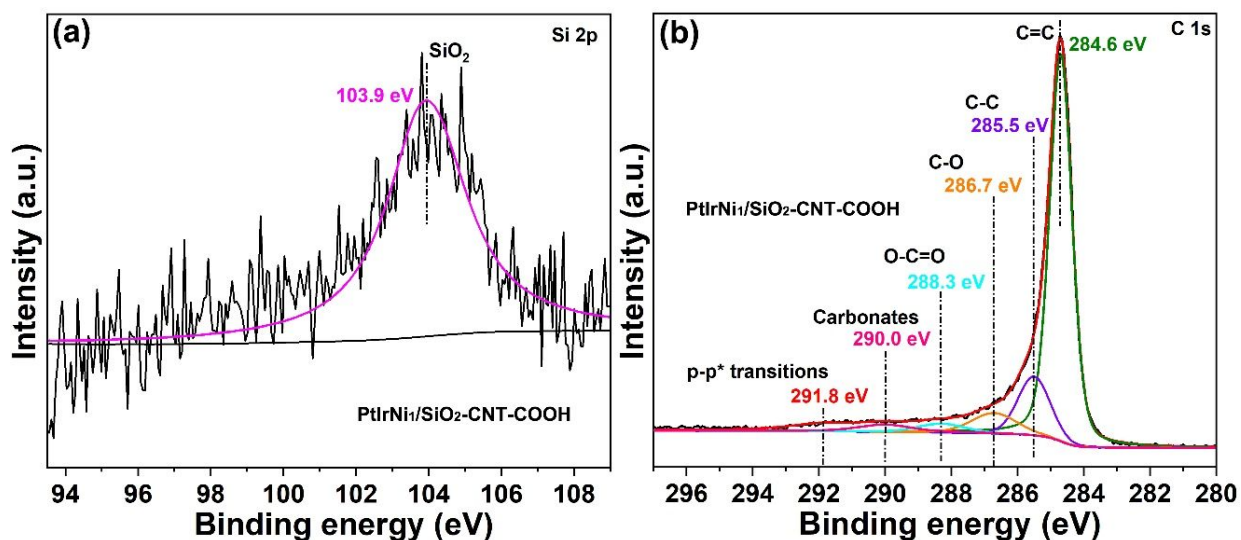


Figure S11. High-resolution XPS data. (a) Si 2p and (b) C 1s of the optimal the PtIrNi₁/SiO₂-CNT-COOH catalyst. This suggests the possible shifts of banding energies for the binary support of SiO₂ and CNT-COOH in the catalysts.

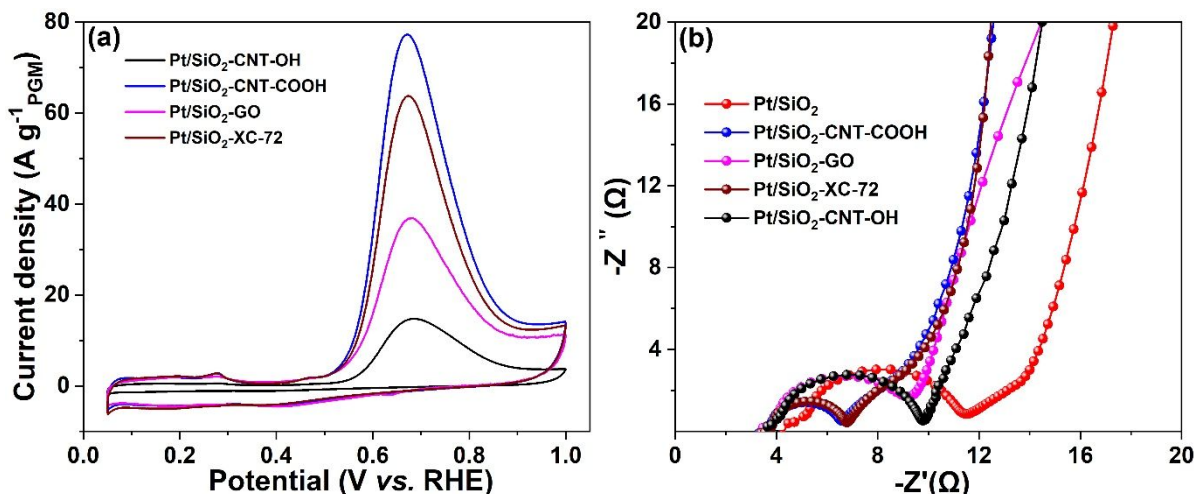


Figure S12. CV curves for different catalysts in Ar-saturated 1.0 M KOH + 0.1 M NH₃ at 5 mV s⁻¹ and 900 rpm under ambient conditions, comparison between Pt deposited on SiO₂ combined with CNT-COOH, CNT-OH, GO, and XC-72 (a), indicating the superiority of combination SiO₂ with CNT-COOH for Pt deposition. Nyquist plots of EIS spectra measured for Pt/SiO₂, Pt/SiO₂-CNT-COOH, Pt/SiO₂-GO, Pt/SiO₂-XC-72, and Pt/SiO₂-CNT-OH in 1.0 M KOH electrolyte at the open circuit potential (b). EIS results indicate the smallest charge transfer resistance of the Pt/SiO₂-CNT-COOH.

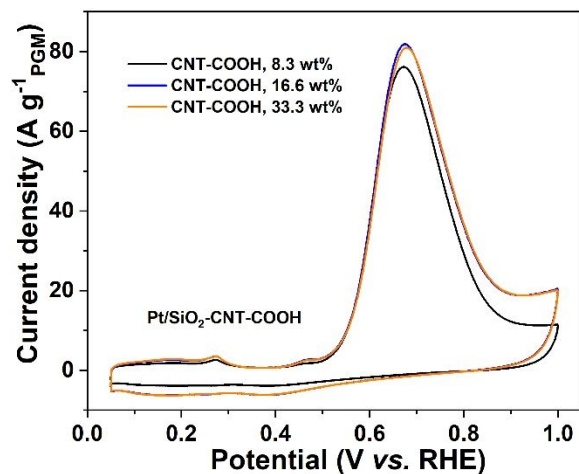


Figure S13. CV curves for different catalysts in Ar-saturated 1.0 M KOH + 0.1 M NH₃ at 5 mV s⁻¹ and 900 rpm under ambient conditions, comparison between Pt deposited on SiO₂ + CNT-COOH with different CNT-COOH contents, suggesting 16.6 wt% CNTs in the support leads to the highest AOR activity.

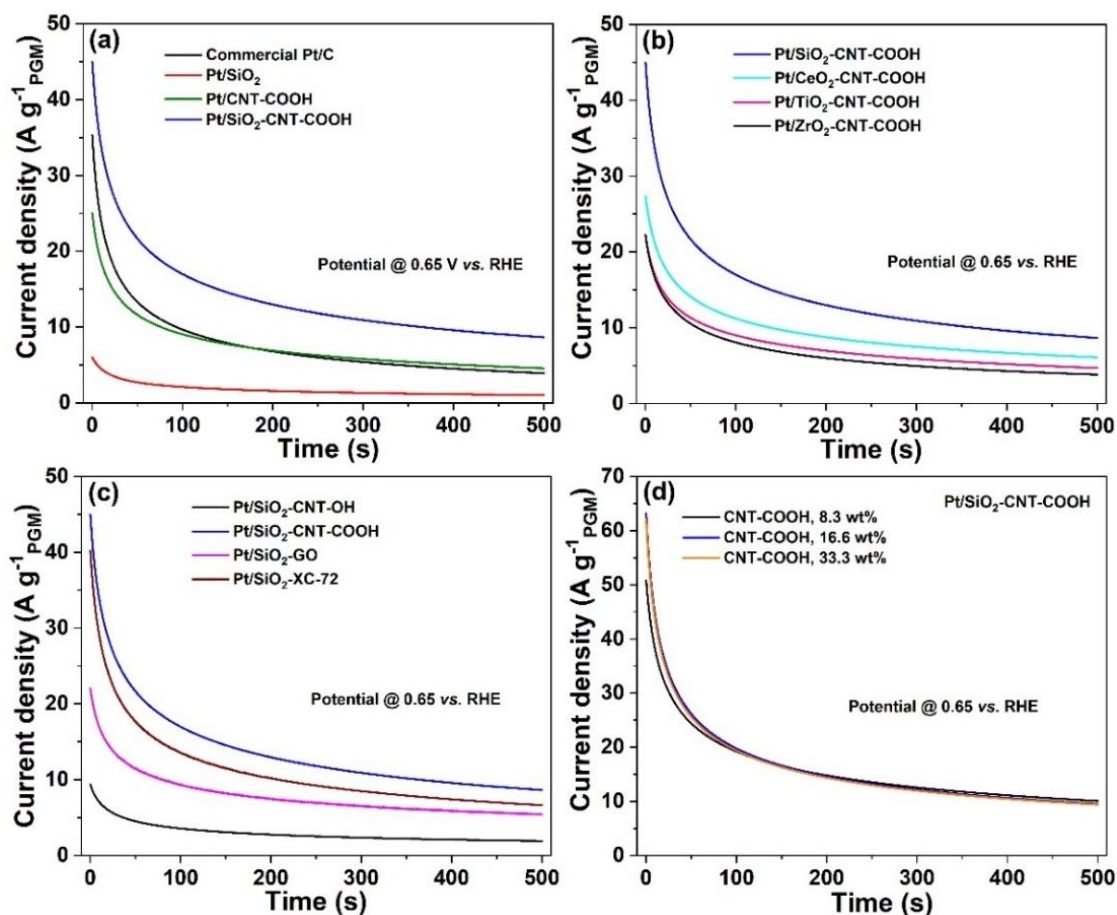


Figure S14. Chronoamperograms (CA) of the different catalysts in Ar-saturated 1.0 M KOH + 0.1 M NH₃ at 900 rpm and 0.65 V vs. RHE under ambient conditions: (a) Comparison between commercial Pt/C, Pt/SiO₂, Pt/CNT-COOH, and Pt/SiO₂-CNT-COOH, (b) Comparison between Pt deposited on CNT-COOH combined with SiO₂, CeO₂, TiO₂, and ZrO₂, (c) Comparison between Pt deposited on SiO₂ combined with CNT-COOH, CNT-OH, GO, and XC-72, and (d) Comparison between Pt deposited on SiO₂-CNT-COOH with different CNT-COOH contents. Chronoamperograms suggest the superiority of combination porous SiO₂ with CNT-COOH for Pt nanoparticle deposition for AOR, better than the commercial Pt/C catalyst.

Table S3. AOR activity comparison of these different catalysts.

Samples	Onset potential (V vs. RHE)	Current density ($A g^{-1}$) at 0.5 V vs. RHE	Peak current density ($A g^{-1}$)
Commercial Pt/C	0.496	–	62.7
Pt/SiO ₂ -CNT-COOH	0.484	–	77.3
Commercial PtIr/C	0.428	10.4	25.1
PtIr/SiO ₂ -CNT-COOH	0.446	8.53	90.6
PtNi/SiO ₂ -CNT-COOH	0.455	4.47	79.2
PtIrNi ₁ /SiO ₂ -CNT-COOH	0.399	13.2	124.0
PtIrNi ₂ /SiO ₂ -CNT-COOH	0.395	16.0	65.4
PtIrNi ₃ /SiO ₂ -CNT-COOH	0.379	11.0	37.0

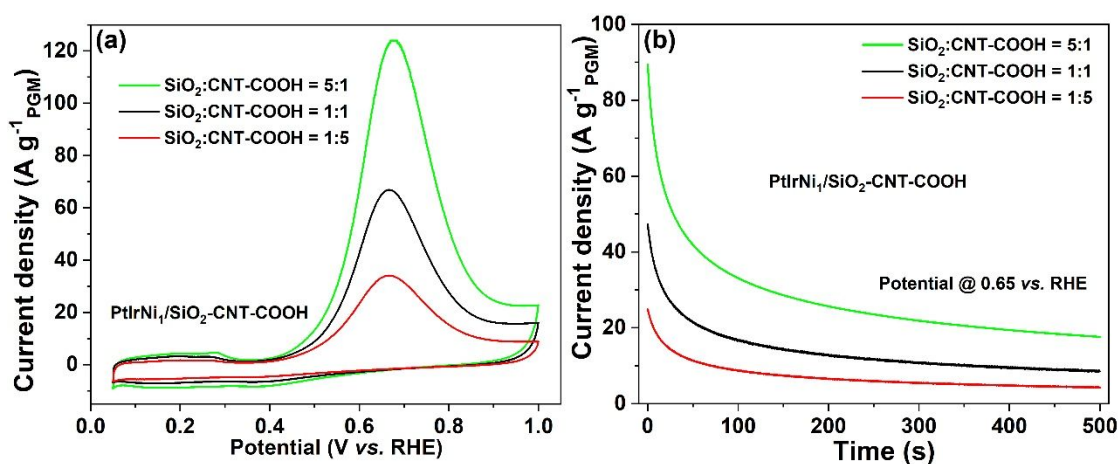


Figure S15. CV curves of the PtIrNi₁/SiO₂-CNT-COOH electrode with different mass ratios (5:1, 1:1, and 1:5) between SiO₂ and CNT-COOH in Ar-saturated 1.0 M KOH + 0.1 M NH₃ electrolyte at 5 mV s⁻¹ and 900 rpm (a), the corresponding Chronoamperograms comparison at the potential of 0.65 V vs. RHE (b). These results suggest that an appropriate mass ratio of 5:1 between SiO₂ and CNT-COOH could result in best AOR activity, and further confirm the critical role of SiO₂ in catalyst synthesis and the contribution of AOR activity enhancement.

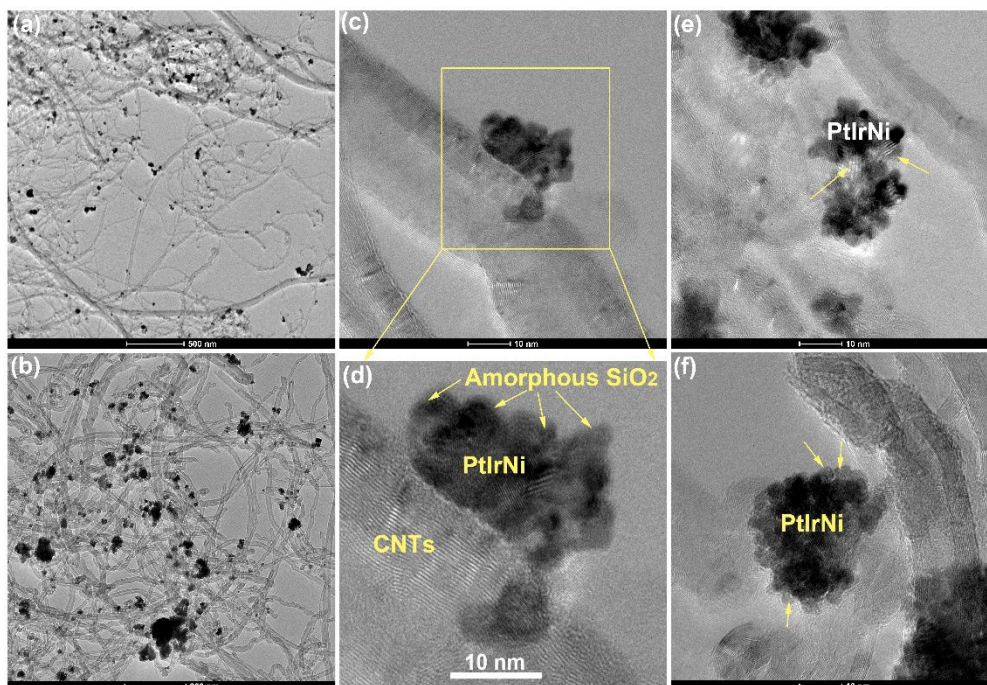


Figure S16. Morphology, structure and composition of the PtIrNi₁/SiO₂-CNT-COOH with a mass ratio of SiO₂:CNT-COOH = 1:1, (a, b) TEM images, and (c-f) HR-TEM images. These images show that clear interfaces between SiO₂ and PtIrNi which are the key active sites contribution.

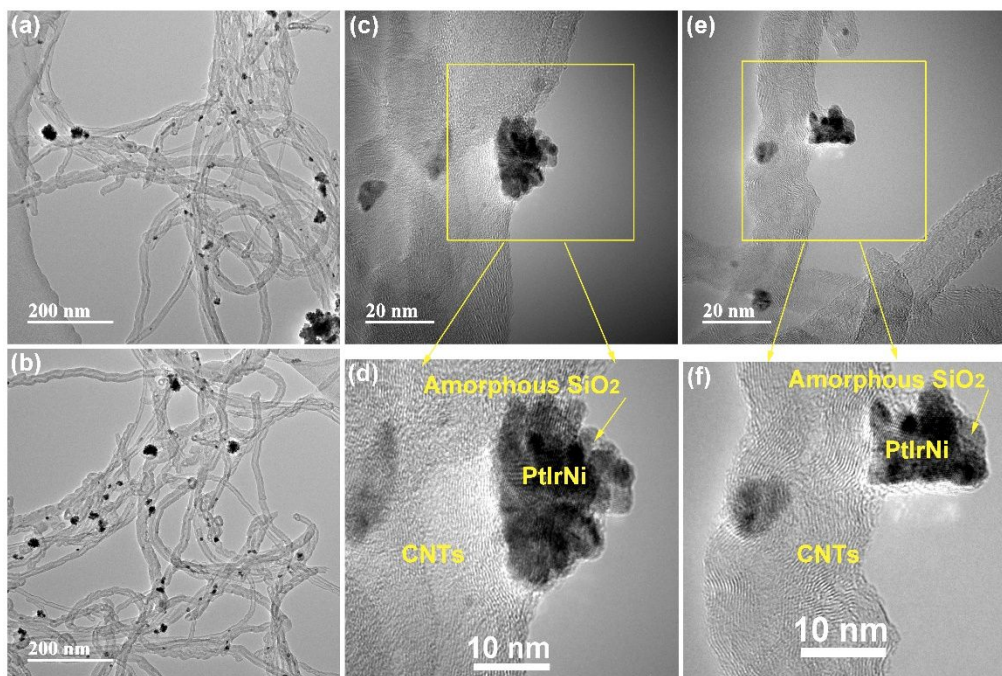


Figure S17. Morphology, structure and composition of the PtIrNi₁/SiO₂-CNT-COOH with a mass ratio of SiO₂:CNT-COOH = 1:5, (a, b) TEM images, and (c-f) HR-TEM images. These images show that clear interfaces between SiO₂ and PtIrNi which are the key active sites contribution.

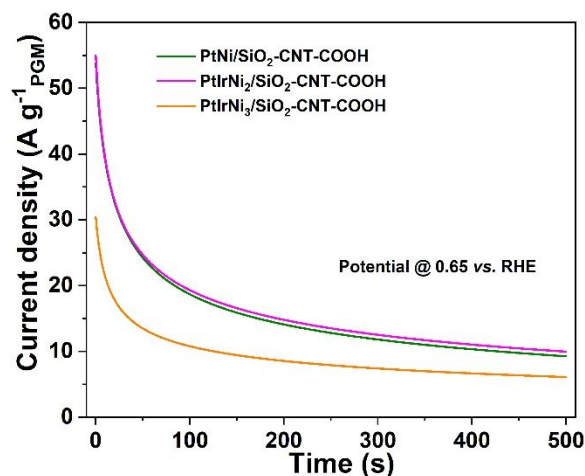


Figure S18. Chronoamperograms comparison between PtNi, PtIrNi₂, PtIrNi₃ deposited on SiO₂-CNT-COOH in Ar-saturated 1.0 M KOH + 0.1 M NH₃ at 900 rpm and the potential of 0.65 V vs. RHE under ambient conditions. CAs (**Figure 6f** and **Figure S16**) further illuminate the best catalytic activity of the PtIrNi₁/SiO₂-CNT-COOH for NH₃ oxidation.

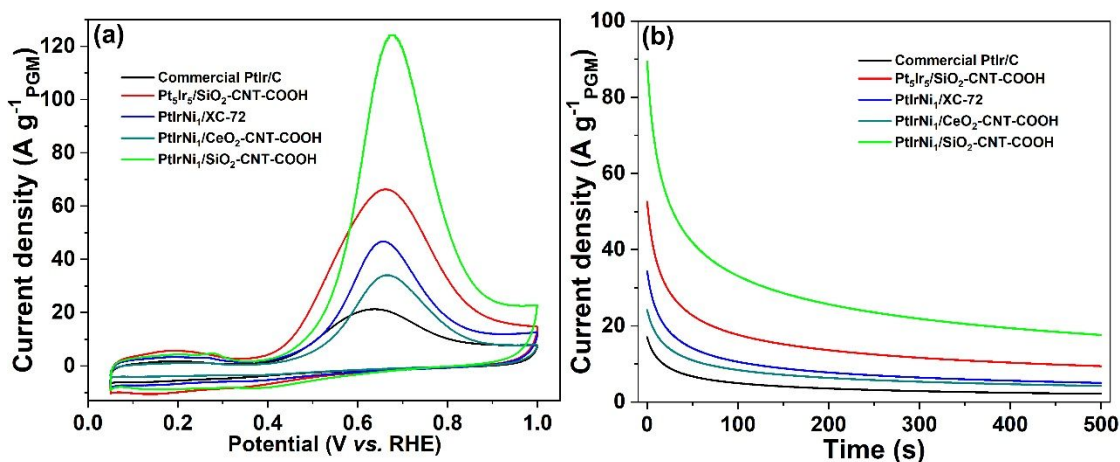


Figure S19. (a) CV curves comparison between commercial PtIr/C, Pt₅Ir₅/SiO₂-CNT-COOH, PtIrNi₁/XC-72, PtIrNi₁/CeO₂-CNT-COOH, and PtIrNi₁/SiO₂-CNT-COOH in Ar-saturated 1.0 M KOH + 0.1 M NH₃ at 5 mV s⁻¹ and 900 rpm under ambient conditions, and (b) their corresponding chronoamperograms. The Pt₅Ir₅/SiO₂-CNT-COOH (molar ratio of Pt:Ir = 1:1) catalyst shows further reduced potential (**Figure 6c** and **Figure S17**), suggesting the significant role of introduced Ir content for lowering the onset potential of the catalyst. Superiority of combination the porous SiO₂ and CNT-COOH can be further demonstrated from this AOR polarization results. The chronoamperogram results are in good agreement with the AOR polarization results.

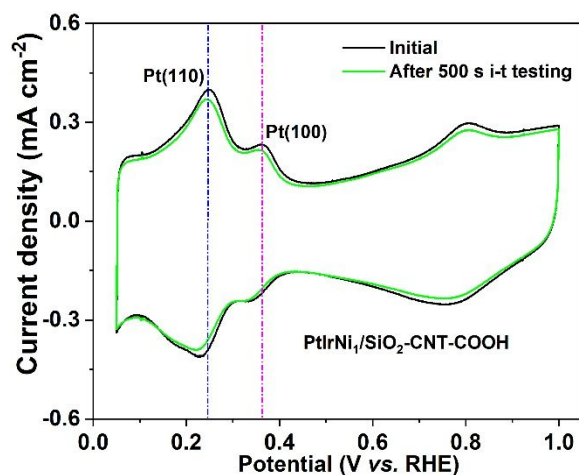


Figure S20. CV curves of the PtIrNi₁/SiO₂-CNT-COOH electrode in 1.0 M KOH before and after 500 s i-t testing (electrolyte: 1.0 M KOH + 0.1 M NH₃; potential: 0.65 V vs. RHE) at a scan rate of 20 mV s⁻¹, note: a reduction potential (−0.8 V vs. SHE) holding for 100 s was used to recover the catalyst. Results indicate that the catalyst deactivation happens during a constant AOR process.

Table S4. AOR activity comparison of these different catalysts.

Samples	Onset potential (V vs. RHE)	Current density (A g ⁻¹) at 0.5 V vs. RHE	Peak current density (A g ⁻¹)	References
PtIrNi ₁ /SiO ₂ -CNT-COOH	0.399	13.2	124.0	This work
Pt ₅ Ir ₅ /SiO ₂ -CNT-COOH	0.369	22.9	66.3	This work
PtIrNi ₁ /CeO ₂ -CNT-COOH	0.465	5.4	34.0	This work
PtIrNi ₁ /XC-72	0.428	8.6	46.7	This work
CeO ₂ -modified Pt	~0.50	–	–	9
Pt-decorated Ni particles	~0.50	–	75.3	10
PtIr/CNT (Pt:Ir = 4:1)	~0.38	–	–	11
PtIr/N-rGO (Pt:Ir = 1:3)	~0.37	–	–	12
PtRh/C (Pt:Rh = 9:1)	~0.44	9.0	93.8	13
CuPtRu (Pt:Ru = 7:1)	~0.49	10.0	180.0	14
PtIrZn (Pt:Ir = 8:2)	~0.30	–	–	15

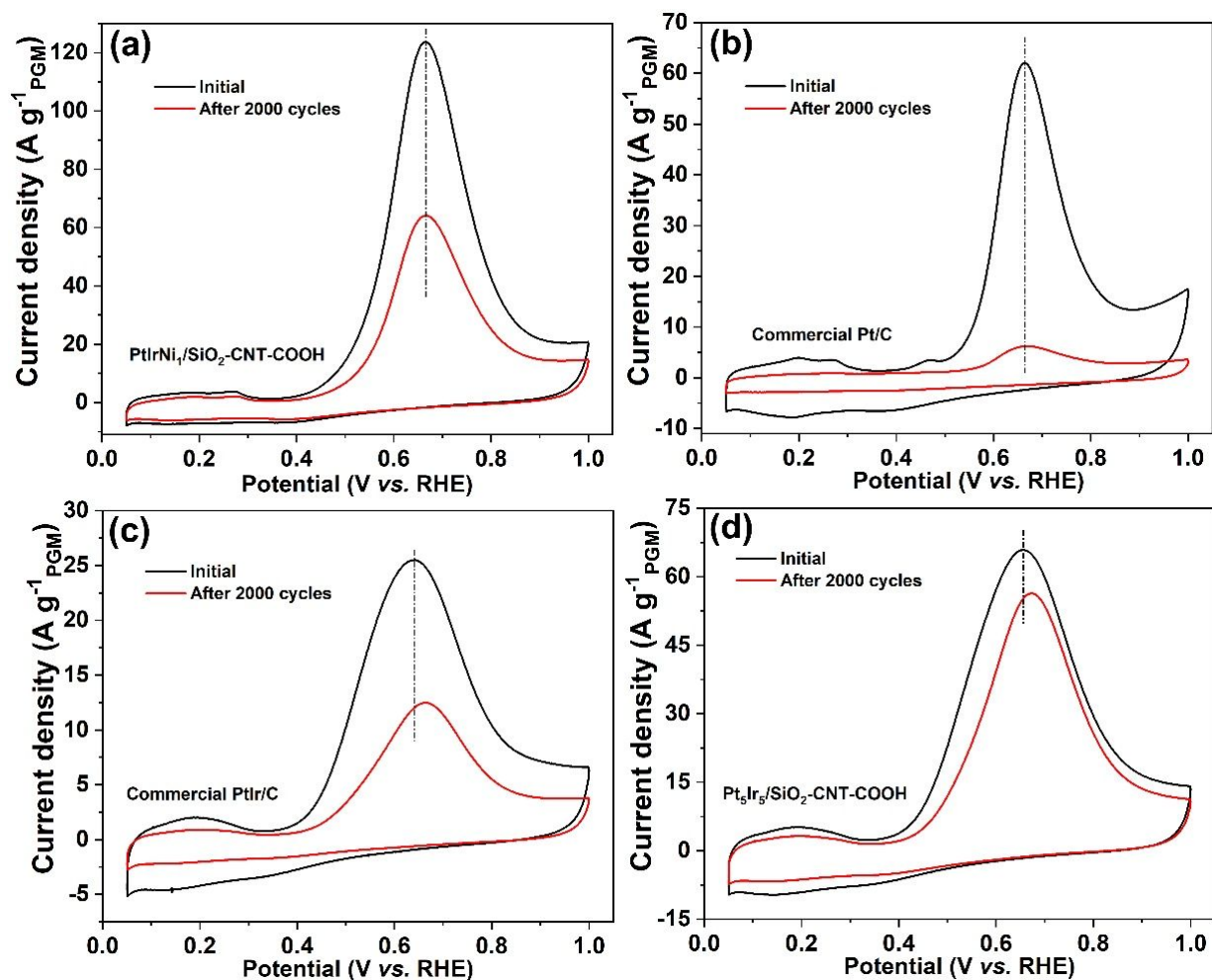


Figure S21. AOR stability tests by cycling the potential of 0.05–0.7 V vs. RHE in Ar-saturated 1.0 M KOH. CV curves before and after 2000 cycles were recorded in 1.0 M KOH + 0.1 M NH₃ at 5 mV s⁻¹ and 900 rpm under ambient conditions. (a) PtIrNi₁/SiO₂-CNT-COOH, (b) commercial Pt/C, (c) commercial PtIr/C, and (d) Pt₅Ir₅/SiO₂-CNT-COOH. AOR stability results indicate that the combination of PtIrNi alloy with binary support of SiO₂ and CNT-COOH can improve AOR stability. Further improving the AOR stability of the Pt-based catalysts can be realized by increasing the Ir content in the Pt-Ir alloy, as demonstrated by the Pt₅Ir₅/SiO₂-CNT-COOH in molar ratio of Pt:Ir = 1:1, which shows a loss of only ~15%.

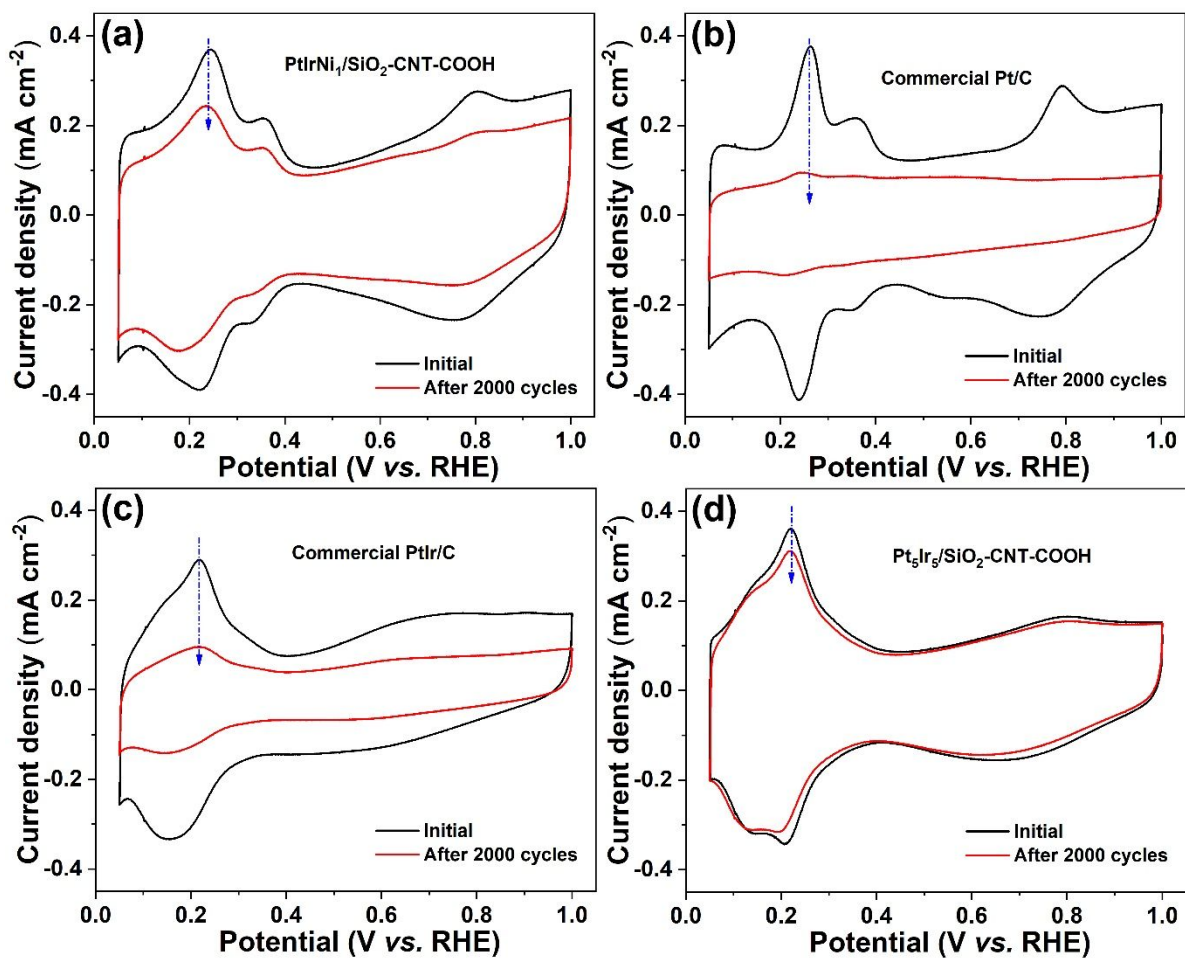


Figure S22. Catalyst degradation tests by cycling the potential of 0.05–0.7 V vs. RHE in Ar-saturated 1.0 M KOH. CV curves before and after 2000 cycles were recorded in 1.0 M KOH at 20 mV s⁻¹ and 900 rpm under ambient conditions. (a) PtIrNi₁/SiO₂-CNT-COOH, (b) commercial Pt/C, (c) commercial PtIr/C, and (d) Pt₅Ir₅/SiO₂-CNT-COOH. Obvious ECSA loss can be observed from these CV curves, indicating the improved resistance to catalyst degradation of PtIrNi and PtIr deposited on SiO₂ + CNT-COOH binary support than the commercial Pt/C and PtIr/C catalysts.

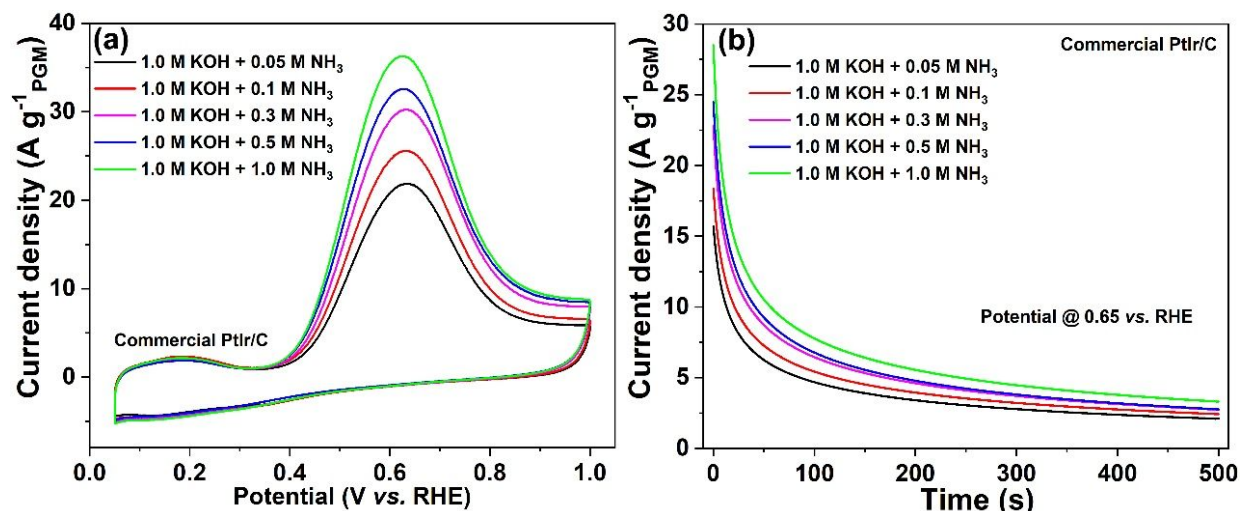


Figure S23. (a) CV curves of the commercial PtIr/C in Ar-saturated 1.0 M KOH in the presence of different concentrations of NH₃ at 5 mV s⁻¹ and 900 rpm under ambient conditions, and (b) the corresponding chronoamperograms. The AOR activity as a function of NH₃ concentration on the commercial PtIr/C catalyst also displays increased activity with the increased NH₃ concentration.

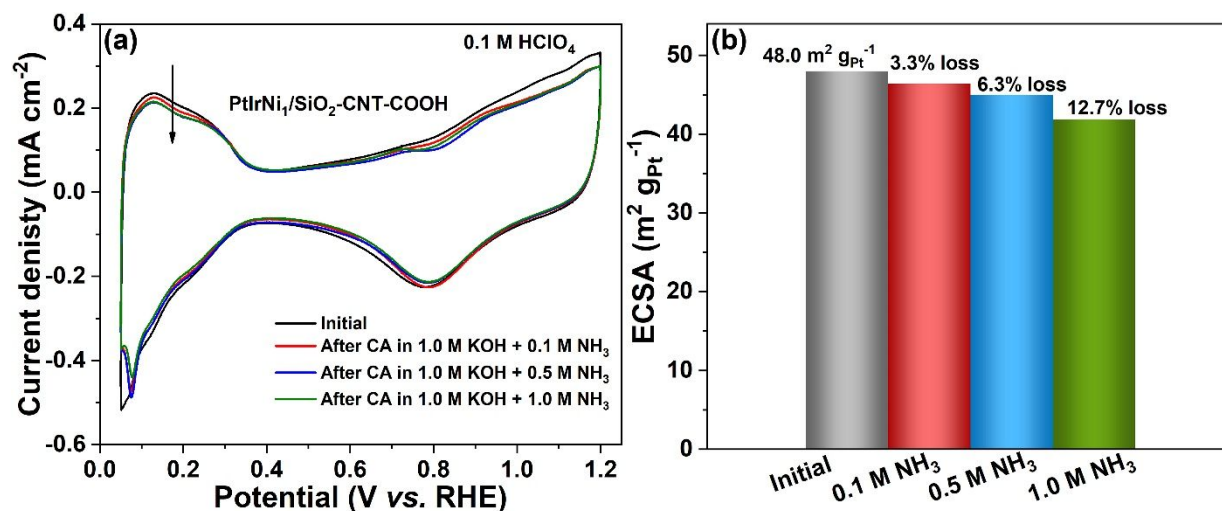


Figure S24. CV curves for PtIrNi₁/SiO₂-CNT-COOH catalyst in Ar-saturated 0.1 M HClO₄ at 20 mV s⁻¹ and 200 rpm under ambient conditions after a constant CA test for 500 s in 1.0 M KOH with 0.1, 0.5, and 1.0 M NH₃, respectively (a), their corresponding ECSA loss (b). The loss of ECSA demonstrate that more poisonous adsorbates could be accumulated in an electrolyte with higher NH₃ concentration during a constant CA test.

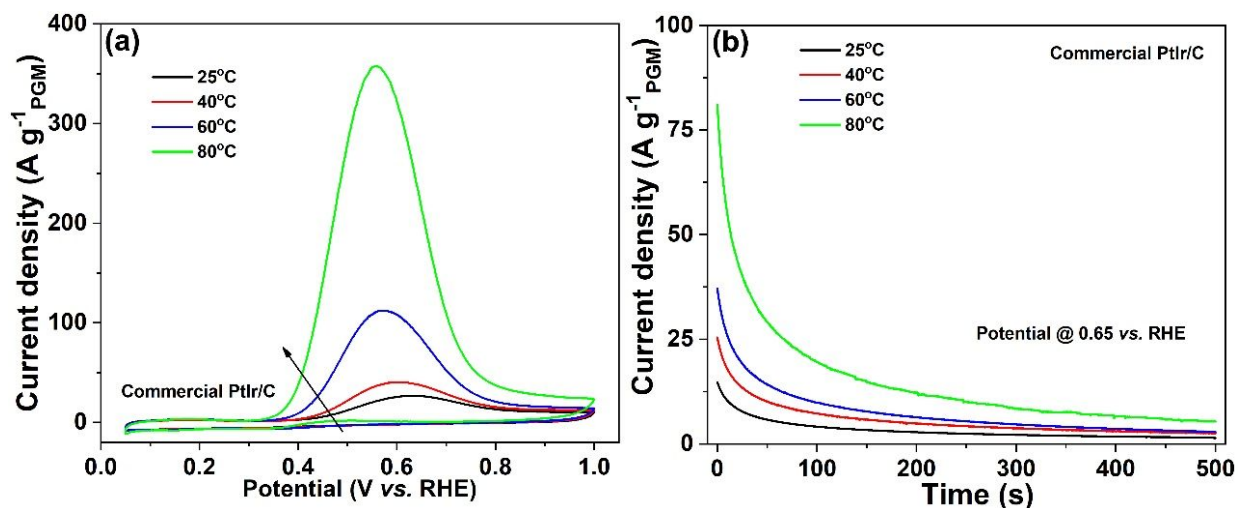


Figure S25. (a) CV curves of the commercial PtIr/C in Ar-saturated 1.0 M KOH + 0.1 M NH₃ at different operation temperatures at 5 mV s⁻¹ and 900 rpm, and (b) the corresponding chronoamperograms. The AOR activity as a function of operation temperature on the commercial PtIr/C catalyst also shows increased activity with the elevated operation temperature.

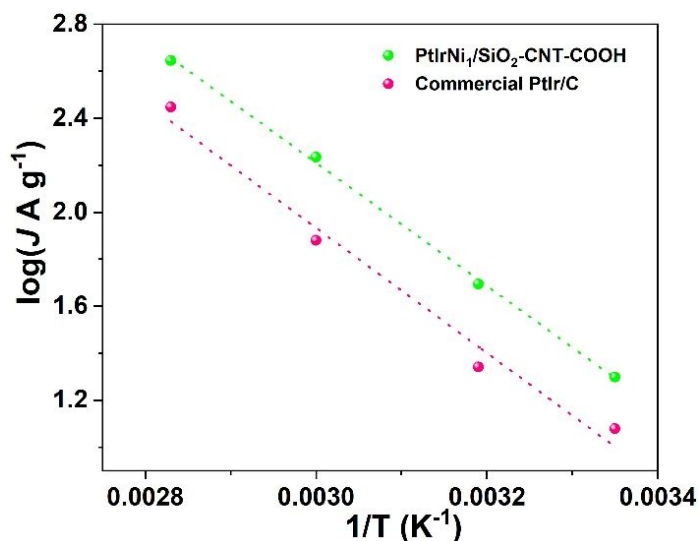


Figure S26. Arrhenius plots for NH₃ oxidation on PtIrNi₁/SiO₂-CNT-COOH and commercial PtIr/C catalysts at the potential of 0.5 V vs. RHE. The calculated ΔH_e value of PtIrNi₁/SiO₂-CNT-COOH is 50.0 kJ mol⁻¹ at 0.5 V, comparable to the commercial PtIr/C (50.8 kJ mol⁻¹), suggesting that lower Ir content in the ternary catalyst does not increase the activation energy of the AOR.

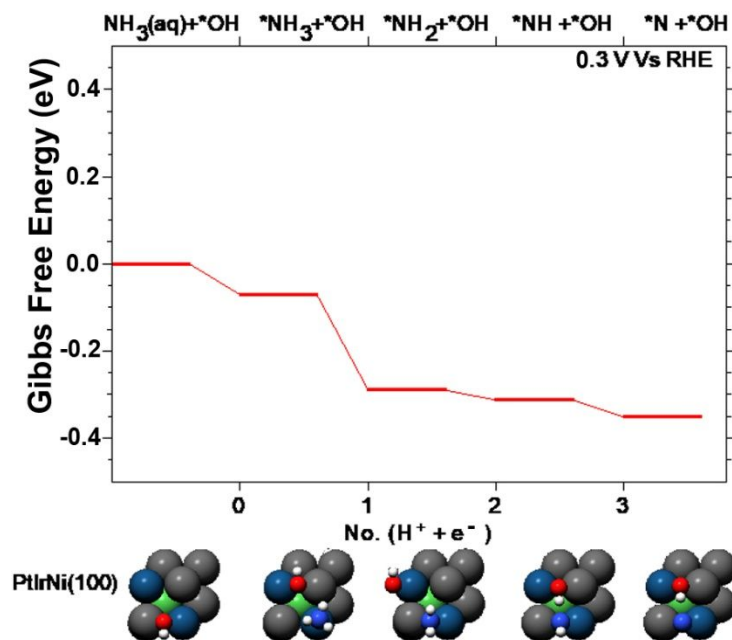


Figure S27. Free energy pathway via constant potential DFT calculations for ammonia dehydrogenation steps at 0.3 V vs. RHE on PtIrNi (100) with subsurface nickel. The geometries for all adsorbates are shown and have coadsorbed *OH (1/4 ML).

Table S5. Segregation Energy for Nickel atom from subsurface to surface.

Ni Segregation Energy (eV)	
Clean	0.521
NH ₃ * + OH*	0.359
NH ₂ * + OH*	0.082
NH* + OH*	0.052
N* + OH*	0.060

References

1. Ding, K.; Gulec, A.; Johnson, A. M.; Drake, T. L.; Wu, W.; Lin, Y.; Weitz, E.; Marks, L. D.; Stair, P. C., Highly efficient activation, regeneration, and active site identification of oxide-based olefin metathesis catalysts. *ACS Catal.* **2016**, *6*, 5740-5746.
2. Ding, K.; Cullen, D. A.; Zhang, L.; Cao, Z.; Roy, A. D.; Ivanov, I. N.; Cao, D., A general synthesis approach for supported bimetallic nanoparticles via surface inorganometallic chemistry. *Science* **2018**, *362*, 560-564.
3. Lee, G.-W.; Kim, J.; Yoon, J.; Bae, J.-S.; Shin, B. C.; Kim, I. S.; Oh, W.; Ree, M., Structural characterization of carboxylated multi-walled carbon nanotubes. *Thin Solid Films* **2008**, *516*, 5781-5784.
4. Goodpaster, J. D.; Bell, A. T.; Head-Gordon, M., Identification of possible pathways for C-C bond formation during electrochemical reduction of CO₂: new theoretical insights from an improved electrochemical model. *J. Phys. Chem. Lett.* **2016**, *7*, 1471-7.
5. Mathew, K.; Sundararaman, R.; Letchworth-Weaver, K.; Arias, T. A.; Hennig, R. G., Implicit solvation model for density-functional study of nanocrystal surfaces and reaction pathways. *J. Chem. Phys.* **2014**, *140*, 084106.
6. Mathew, K.; Hennig, R. G., Implicit self-consistent description of electrolyte in plane-wave density-functional theory. *arXiv preprint arXiv* **2016**, *1601*, 03346.
7. Pillai, H. S.; Xin, H., New insights into electrochemical ammonia oxidation on Pt(100) from first principles. *Ind. Eng. Chem. Res.* **2019**, *58*, 10819-10828.
8. Slater, J. C.; Koster, G. F., Simplified LCAO method for the periodic potential problem. *Phys. Rev.* **1954**, *94*, 1498-1524.
9. Katayama, Y.; Okanishi, T.; Muroyama, H.; Matsui, T.; Eguchi, K., Enhanced supply of hydroxyl species in CeO₂-modified platinum catalyst studied by in situ ATR-FTIR spectroscopy. *ACS Catal.* **2016**, *6*, 2026-2034.
10. Liu, J.; Chen, B.; Kou, Y.; Liu, Z.; Chen, X.; Li, Y.; Deng, Y.; Han, X.; Hu, W.; Zhong, C., Pt-decorated highly porous flower-like Ni particles with high mass activity for ammonia electro-oxidation. *J. Mater. Chem. A* **2016**, *4*, 11060-11068.
11. Morita, S.; Kudo, E.; Shirasaka, R.; Yonekawa, M.; Nagai, K.; Ota, H.; N.-Gamo, M.; Shiroishi, H., Electrochemical oxidation of ammonia by multi-wall-carbon-nanotube-supported Pt shell-Ir core nanoparticles synthesized by an improved Cu short circuit deposition method. *J. Electroanal. Chem.* **2016**, *762*, 29-36.
12. Zhou, Y.; Zhang, G.; Yu, M.; Xu, J.; Qiao, S.; Cheng, X.; Yang, F., High mass and specific activity for ammonia electro-oxidation through optimization of dispersion degree and particle size of Pt-Ir nanoparticles over N-doped reductive graphene oxide. *ChemistrySelect* **2018**, *3*, 3433-3443.
13. Assumpção, M. H. M. T.; Piasentin, R. M.; Hammer, P.; De Souza, R. F. B.; Buzzo, G. S.; Santos, M. C.; Spinacé, E. V.; Neto, A. O.; Silva, J. C. M., Oxidation of ammonia using PtRh/C electrocatalysts: fuel cell and electrochemical evaluation. *Appl. Catal., B* **2015**, *174-175*, 136-144.
14. Manso, R. H.; Song, L.; Liang, Z.; Wang, J. X.; Chen, J., CuPt and CuPtRu nanostructures for ammonia oxidation reaction. *ECS Trans.* **2018**, *85*, 177-182.
15. Jiang, J., Promotion of PtIr and Pt catalytic activity towards ammonia electrooxidation through the modification of Zn. *Electrochem. Commun.* **2017**, *75*, 52-55.